

Imaging and modelling the impact of multi-scale pore connectivity on two-phase flow in mixed-wet rock

Shan Wang¹, Arjen Mascini¹, Leonardo C. Ruspini², Paal Eric Oren³, and Tom Bultreys¹

¹Ghent University

²Petricore Norway AS

³Petricore Norway

December 17, 2022

Abstract

The wetting properties of pore walls have a strong effect on multiphase flow through porous media. However, the fluid flow behaviour in porous materials with both complex pore structures and non-uniform wettability are still unclear. Here, we performed unsteady-state quasi-static oil- and waterflooding experiments to study multiphase flow in two sister heterogeneous sandstones with variable wettability conditions (i.e. one natively water-wet and one chemically treated to be mixed-wet). The pore-scale fluid distributions during this process were imaged by laboratory-based X-ray micro-computed tomography (micro-CT). In the mixed-wet case, we observed pore filling events where the fluid interface appeared to be at quasi-equilibrium at every position along the pore body (13% by volume), in contrast to capillary instabilities typically associated with slow drainage or imbibition. These events corresponded to slow displacements previously observed in unsteady-state experiments, explaining the wide range of displacement time scales in mixed-wet samples. Our new data allowed us to quantify the fluid saturations below the image resolution, indicating that slow events were caused by the presence of microporosity and the wetting heterogeneity. Finally, we investigated the sensitivity of the multi-phase flow properties to the slow filling events using a state-of-the-art multi-scale pore network model. This indicated that pores where such events took place contributed up to 19% of the sample's total absolute permeability, but that the impact on the relative permeability may be smaller. Our study sheds new light on poorly understood multiphase fluid dynamics in complex rocks, of interest to e.g. groundwater remediation and subsurface CO₂ storage.

Hosted file

952101_0_art_file_10533368_rmcggl.docx available at <https://authorea.com/users/539115/articles/613611-imaging-and-modelling-the-impact-of-multi-scale-pore-connectivity-on-two-phase-flow-in-mixed-wet-rock>

Hosted file

952101_0_supp_10533370_rm4gg1.docx available at <https://authorea.com/users/539115/articles/613611-imaging-and-modelling-the-impact-of-multi-scale-pore-connectivity-on-two-phase-flow-in-mixed-wet-rock>

15 **Abstract**

16 The wetting properties of pore walls have a strong effect on multiphase flow through porous
17 media. However, the fluid flow behaviour in porous materials with both complex pore
18 structures and non-uniform wettability are still unclear. Here, we performed unsteady-state
19 quasi-static oil- and waterflooding experiments to study multiphase flow in two sister
20 heterogeneous sandstones with variable wettability conditions (i.e. one natively water-wet and
21 one chemically treated to be mixed-wet). The pore-scale fluid distributions during this process
22 were imaged by laboratory-based X-ray micro-computed tomography (micro-CT). In the
23 mixed-wet case, we observed pore filling events where the fluid interface appeared to be at
24 quasi-equilibrium at every position along the pore body (13% by volume), in contrast to
25 capillary instabilities typically associated with slow drainage or imbibition. These events
26 corresponded to slow displacements previously observed in unsteady-state experiments,
27 explaining the wide range of displacement time scales in mixed-wet samples. Our new data
28 allowed us to quantify the fluid saturations below the image resolution, indicating that slow
29 events were caused by the presence of microporosity and the wetting heterogeneity. Finally,
30 we investigated the sensitivity of the multi-phase flow properties to the slow filling events
31 using a state-of-the-art multi-scale pore network model. This indicated that pores where such
32 events took place contributed up to 19% of the sample's total absolute permeability, but that
33 the impact on the relative permeability may be smaller. Our study sheds new light on poorly
34 understood multiphase fluid dynamics in complex rocks, of interest to e.g. groundwater
35 remediation and subsurface CO₂ storage.

36 **1 Introduction**

37 Immiscible two-phase flow through porous media is very common in natural subsurface
38 systems. A thorough understanding of fluid flow mechanisms has crucial applications in
39 geological CO₂ sequestration (Shukla et al., 2010), contaminated groundwater remediation
40 (Kalhor et al., 2019) and subsurface energy storage (Panfilov, 2010). In recent years, in order
41 to better characterize the intricate internal pore structures of porous materials, advanced
42 imaging techniques such as X-ray micro-computed tomography (micro-CT) have been widely
43 applied in the laboratory (Chen et al., 2021; Gao et al., 2019; Iglauer et al., 2011; Lin et al.,
44 2021; Offenwert et al., 2019). The combination of X-ray micro-CT imaging with flow
45 experiments has greatly facilitated the study of multiphase flow behavior at the pore scale.
46 High-resolution images can provide important information to quantify the flow properties
47 including fluid distributions (Lin et al., 2021), fluid flow dynamics (Reynolds et al., 2017;
48 Singh et al., 2022; Spurin et al., 2019), filling characteristics (Bultreys et al., 2018; Gao et al.,
49 2020), interfacial properties (Garing et al., 2017; Herring et al., 2017; Zankoor et al., 2021),
50 etc., which cannot be measured in traditional core flooding experiments.

51 Wettability is known to play a crucial role in multiphase flow through porous rocks. It controls
52 the fluid invasion sequences and the fluid distribution state in the pore network, which in turn
53 influences the constitutive properties used in continuum models, for example capillary pressure
54 and relative permeability. While most minerals are water-wet, the adhesion of surface active
55 components present in e.g. crude oil or certain environmental pollutants can lead to changes in
56 the fluid affinity to the surface, i.e. wettability alteration (Al-Futaisi & Patzek, 2004; Buckley
57 et al., 1998; Gao et al., 2020; Morrow, 1990). For example, in a mixed-wet system pore surfaces
58 in larger pores become hydrophobic due to direct contact with surface active components, while
59 corners, crevices and smaller pores retain water and therefore remain more hydrophilic. This
60 is influenced by a number of factors, including surface roughness, pore morphology, mineral
61 composition, etc. (AlRatrouf et al., 2018b; Garfi et al., 2020). At the pore scale, the resulting
62 wettability alteration is reflected by changes in local contact angles. Recent advances in image
63 processing algorithms have made it possible to quantify this directly on 3D images of the fluid

64 distribution (Andrew et al., 2014; Klise et al., 2016; Scanziani et al., 2017). The contact angle
65 measured on segmented images is usually termed the “geometric contact angle” in literature
66 (Alhammadi et al., 2020). This calculation can be done either manually or automatically. More
67 recently, the thermodynamic contact angle (Blunt et al., 2019), event-based contact angle
68 (Mascini et al., 2020), force-based contact angle (Mascini et al., 2020) and topology-based
69 contact angle (Sun et al., 2020) were proposed to reduce the uncertainty of measuring contact
70 angles during a displacement process.

71 Although significant progress has been achieved in revealing complex fluid dynamics in porous
72 media based on advanced imaging techniques, most research has focused on materials with
73 homogeneous wettability (mostly water-wet state) and simple pore structures (Berg et al., 2013;
74 Datta et al., 2014; Offenwert et al., 2019; Rucker et al., 2015). The fluid flow mechanisms in
75 heterogeneous rocks with non-uniform wetting, in which the pore sizes span from a few
76 nanometers to centimeter scale, are still poorly understood. Alhammadi et al. (2020) and Lin
77 et al. (2021) performed co-injection experiments to measure relative permeability in altered-
78 wettability carbonate samples, but the macroscopic capillary pressure cannot be obtained from
79 this type of experiments. Mascini et al. (2021) recently reported a newly discovered fluid
80 invasion phenomenon in a rock with both structural and wetting heterogeneity: a significant
81 proportion of the pore-scale fluid displacements were observed to be several orders of
82 magnitude slower than the traditional displacement types found in neighboring pores (e.g.
83 Haines jumps). They hypothesized that the complex wettability and pore space architecture
84 changed the local capillary-viscous force balance, which could be the main reason for the
85 concurrence of these slow filling events and fast displacements. However, they only showed
86 the fluid dynamics during waterflooding, and couldn't fully relate the behavior to the effects of
87 microporosity (i.e. the porosity for pores below image resolution). To further explain what
88 causes this filling behavior and how important it is in slow flooding, it is necessary to develop
89 a comprehensive experimental and simulation workflow to study the underlying mechanisms
90 of multiphase flow in geological rocks with complex wettability and pore structures.

91 In this paper, we introduce an experimental procedure that uses both oil-wet and water-wet

92 porous plates to perform unsteady-state capillary oil and waterflooding on heterogeneous
93 sandstone samples in water-wet and mixed-wet conditions, while imaging the pore structures
94 and the fluid invasion characteristics by laboratory-based X-ray micro-CT scanning. By
95 performing the experiments quasi-statically, the quality of the micro-CT images is high enough
96 to quantify microporosity and fluid saturations. Section 2 shows the experimental materials,
97 procedures and data processing workflow. In section 3, we first introduce the observed pore
98 filling behavior in the two samples under quasi-static flooding (section 3.1). The possible
99 reasons leading to the gradually filling behavior in the mixed-wet sample are then analyzed
100 based on the wettability characterization (section 3.2) and the analysis of the pore network
101 characteristics (section 3.3). Section 3.4 provides a novel workflow to investigate the
102 sensitivity of the multiphase flow properties to the slow movement of the fluid menisci, using
103 a state-of-the-art multi-scale pore network model (PNM) for porous media with heterogeneous
104 architecture and wettability distribution.

105 **2 Materials and methods**

106 **2.1 Materials**

107 There were two Luxembourg sandstone samples used in this study. The Luxembourg sandstone
108 is a heterogeneous, calcareous quarried sandstone with complex pore structures, which consist
109 of macropores and a significant fraction of microporosity (Molenaar, 1998). Mercury intrusion
110 porosimetry on a sister sample showed it has a bimodal pore throat size distribution (supporting
111 information Figure S1) centered on 2 μm and 20 μm and a porosity of 18.76% (Mascini et al.,
112 2021). One sample was water-wet (WW) with 20 mm in length and 6 mm in diameter. Another
113 (13 mm in length and 6 mm in diameter) was chemically treated to change the wettability by
114 immersing the cleaned and dried sample in 25 ml of decane with 5 wt.%
115 octadecyltrichlorosilane (OTS) for 24 hours, then cleaning the sample with isopropanol and
116 drying. The treated sample was wrapped in teflon tape and stored in a desiccator. For more
117 details on the wettability treatment, we refer to Mascini et al. (2021).

118 For the experiment, a brine solution made from deionized water doped with 25 wt% potassium

119 iodine (KI) was prepared as the aqueous phase to provide image contrast, so that the fluids in
120 the pores could be distinguished. n-Decane was used as the oil phase.

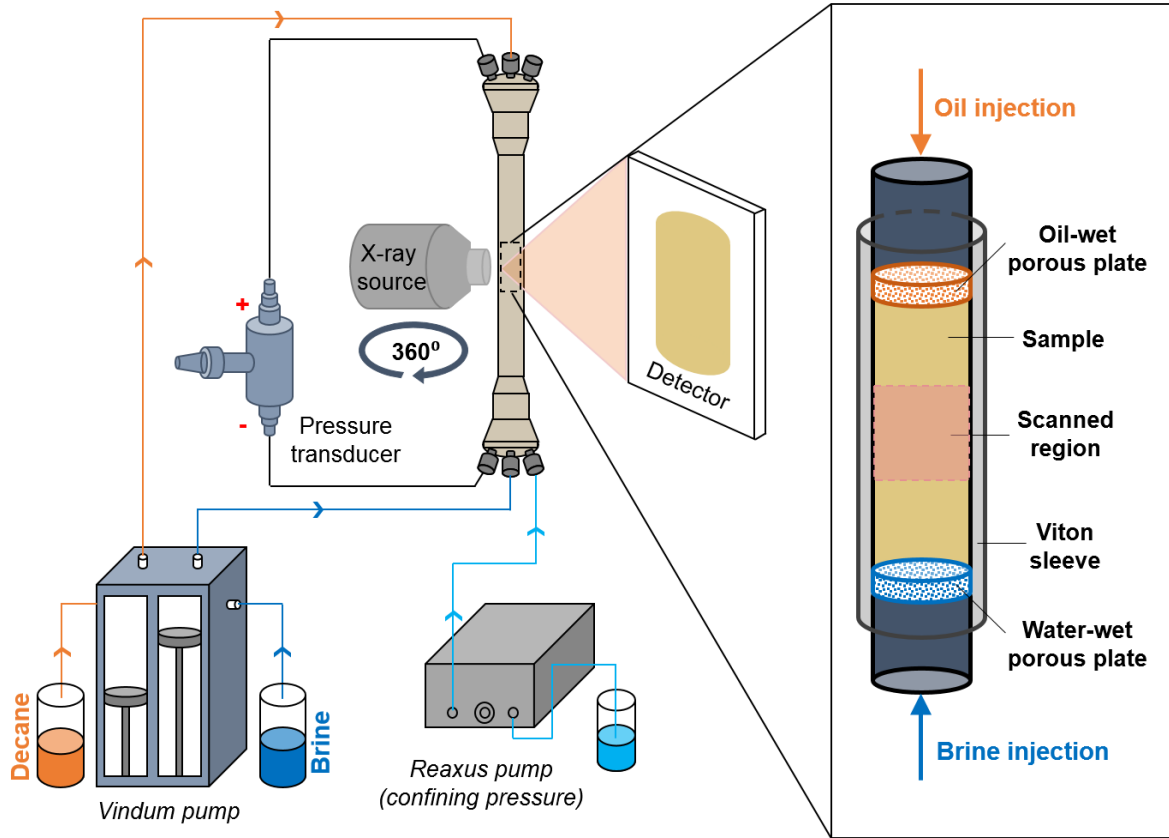
121 **2.2 Flow apparatus and procedure**

122 The aim of the unsteady-state flow experiment performed here was to investigate the fluid
123 invasion and distribution mechanisms during quasi-static oil and water flooding under
124 different wettability conditions. Figure 1 shows the flow apparatus. The sample was placed in
125 a fluoropolymer elastomer (Viton) sleeve with a hydrophobic and a hydrophilic porous plate
126 fitted on its top and bottom, respectively. The tight pore sizes (150 nm in diameter) of the
127 porous plates prevented the early breakthrough of invading fluid (i.e. hydrophobic and
128 hydrophilic porous plates prevented brine and decane passing through at low pressures
129 respectively) and created a relatively homogeneous saturation profile during fluid injection.
130 The two end pieces connected the sample to the flow lines. This assembly was mounted in a
131 PEEK hassler-type flow cell which is X-ray transparent (RS Systems, Norway). A Vindum
132 Engineering VP-12 pump was used to pump the two fluid phases into the samples. The pressure
133 drop over the sample was measured by a differential pressure transducer (Keller PD-33X).

134 The flow cell was mounted in the Environmental Micro-CT (EMCT) scanner at the center for
135 X-ray tomography at Ghent University (UGCT) (Bultreys et al., 2016; Dierick et al., 2014).
136 This is a gantry-based system with a rotating source-and-detector assembly. This ensured that
137 the sample and flow lines were kept static during image acquisition. For the image acquisition,
138 the X-ray tube settings were 110 kV and 8 W, the voxel size was 6.5 μm , and we used a 1.15 s
139 integration time per radiograph for 2400 projections.

140 The experiment consisted of decane injection into a brine saturated sample, followed by brine
141 injection. Both injections took place at low capillary numbers (Ca). The Ca is defined as the
142 ratio of capillary forces to viscous forces ($Ca = \mu q / \sigma$, where μ is the dynamic viscosity of the
143 injected fluid, q is the Darcy velocity, σ is interfacial tension between two fluids. Typically, the
144 system is considered to be capillary dominated flow if Ca is lower than 10^{-6}). For convenience,
145 we will refer to the injection of decane and brine as oil and water flooding in following sections.

146 The confining pressures for both samples were kept at 3800 kPa during the whole process.
147 After taking a dry micro-CT scan, brine was pumped into the samples for several hours, where
148 the pressure drop over the samples was controlled at 3000 ± 100 kPa, to fully displace air inside,
149 and a brine-saturated scan was taken when no more changes were observed in sample. Then,
150 decane was injected slowly (capillary number $< 10^{-9}$) from top to bottom, while the bottom
151 water-wet porous plate prevented the oil phase to pass through. For each sample, a set of
152 controlled, increasing capillary pressure steps were imposed, each by adjusting the flow rate to
153 obtain a constant low differential pressure over the sample and the capillary plates. For the
154 water-wet case, we obtained 4 pressure steps at 2.5, 4, 6 and 27 kPa. For the mixed-wet sample,
155 the capillary pressures were 2, 3.5, 4.5 and 6 kPa. Each pressure step was followed by a micro-
156 CT scan after pumping 12 to 24 hours, when no changes were observed anymore on differential
157 radiographs. Then, the flow was reversed: the decane pump was stopped, and brine was injected
158 from the bottom to the top of the sample at 0.00008 ml/min for the water-wet sample and
159 0.0001 ml/min for the mixed-wet counterpart. Three micro-CT scans during this waterflooding
160 process were taken for each sample, respectively. The top hydrophobic porous plate only
161 allowed oil phase to flow out during this waterflooding process. Note that the reason we used
162 a constant flow rate instead of constant pressure in this process is that for the water-wet sample,
163 the invaded watery fluid always swells from micropores or smaller pores first. This can happen
164 very quickly if the constant pressure is not controlled to a very high accuracy, resulting in fast
165 oil phase trapping and reaching the residual oil saturation state in a short period of time. To
166 avoid this risk, a very low constant flow rate was used in the waterflooding experiments on
167 both samples. Considering that the imbibition in the water-wet sample can be expected to
168 proceed faster than in the mixed-wet sample, we used a slightly lower flow rate for the former,
169 to better record the fluid invasion process.



170

171

Figure 1. Experimental apparatus and detail of assembly inside the flow cell.

172 2.3 Image processing

173 After reconstruction, the Avizo 2020.2 (Thermo Fisher Scientific, France) software was used
 174 for image processing. All the images were registered using normalized mutual information to
 175 a reference scan and resampled with the Lanczos algorithm (Burger & Burge, 2010). This way,
 176 they were aligned in space. Following this, a non-local means edge-preserving filter (Buades
 177 et al., 2008) was applied to all images to reduce the noise. As can be seen in Figure 2, pore-
 178 filling and dissolution microporosity were commonly encountered. Because of the high X-ray
 179 attenuation coefficient of the KI in brine phase, the pores filled with brine had bright grey
 180 values in the images. In order to reduce segmentation errors, macropores were first segmented
 181 manually on the dry scan using histogram thresholding. The differential imaging method
 182 (subtracting dry scans from brine-saturated scans) (Lin et al., 2016; Wang et al., 2022) was
 183 used to identify microporous regions. Then, the rest of the voxels in the dry scan were assigned
 184 as solid grain phase. Figure 2 shows the three phase segmentation results. For multiphase scans,

185 the decane and brine within macropores were also classified with histogram thresholding, on
 186 which the labelled macro-pore space was used as a mask (Wang et al., 2022).

187 The porosity distribution can be calculated based on differential images between the brine
 188 saturated scan and the dry scan with the following equation:

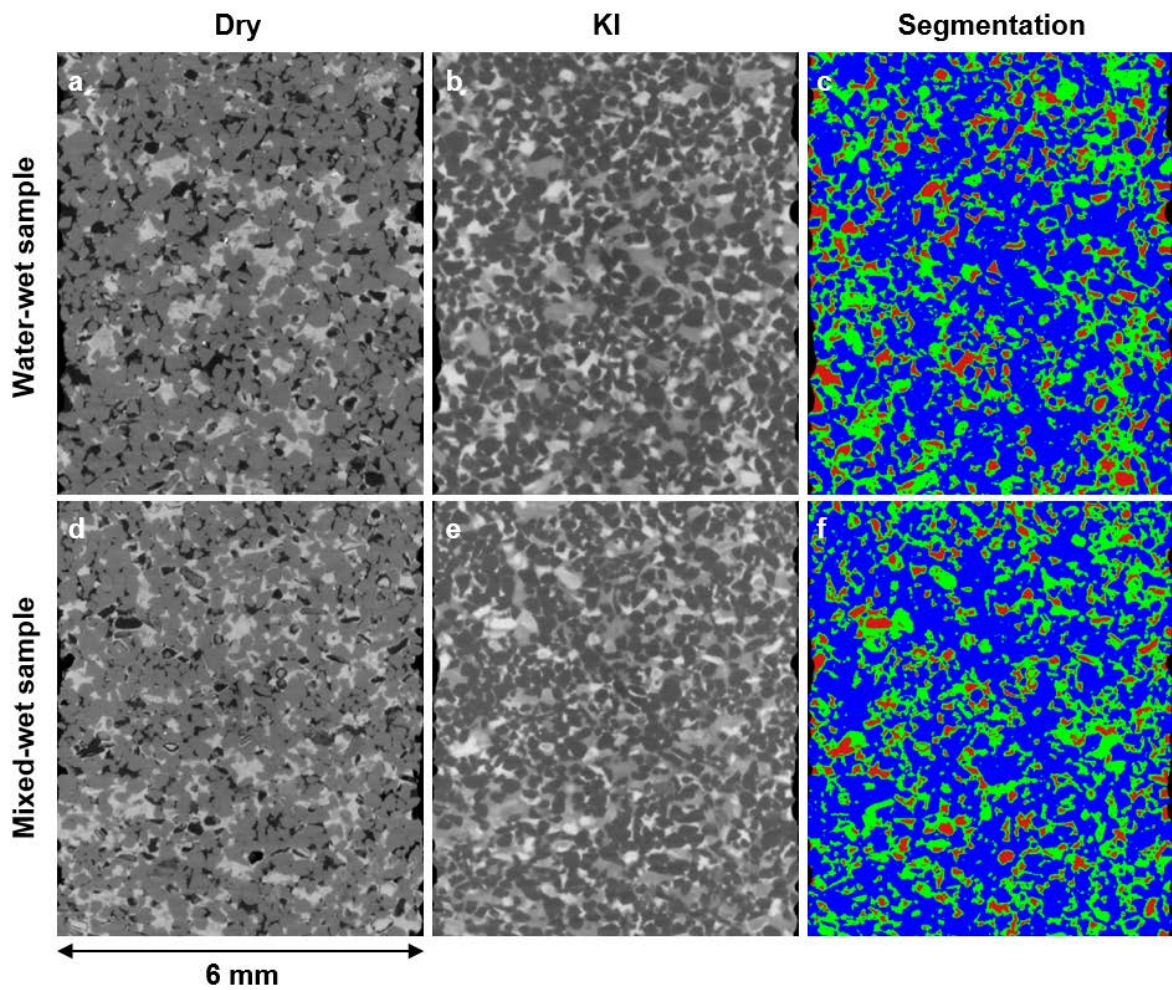
$$189 \quad \varphi_{micro} = \frac{I_{diff} - CT1}{CT2 - CT1} \quad (1)$$

190 where I_{diff} is the grey value difference of two scans, $CT1$ is the threshold value for solid phase
 191 (0% porosity), which was determined based on grey value at the boundary of the solid grain
 192 and microporous region in the histogram, $CT2$ is the threshold value for macropores (100%
 193 porosity), which was obtained by masking segmented macropores on differential image and
 194 finding the peak value existed in the grey value histogram. Similarly, the saturation distribution
 195 map can also be obtained with multiphase-dry differential image. The full details are provided
 196 in our previous publication (Wang et al., 2022).

197 For curvature measurements, the marching cube algorithm was applied on the segmented
 198 waterflooding images to generate triangulated surfaces, which were smoothed by a Gaussian
 199 filter with a constrained smoothing extent of 3 voxels to remove noise and staircase-like
 200 artifacts (Li et al., 2018). Following this, the oil-brine surfaces were extracted and
 201 approximated locally by a quadratic form. The eigenvalues and eigenvectors, which represent
 202 the values and directions of two principal curvatures, of this quadratic form were used to
 203 calculate the mean curvature, i.e. $\kappa = (\kappa_1 + \kappa_2)/2$. Due to the limited image resolution (6.5 μm)
 204 and the complex pore structures, the segmentation on the rough edges of oil-brine interface
 205 near solid material may generate unrealistic curvature values. We followed the procedures
 206 presented in (Mascini et al., 2020) and (Li et al., 2018) to filter data points. The curvatures
 207 which had a radius of curvature value smaller than twice the voxel size, i.e. $\kappa > 1/(2 * \text{voxel size})$,
 208 were first removed as they were likely affected by artifacts. Then, the geodesic distance of each
 209 triangle was calculated by averaging the three shortest vertex distances on it. The distance
 210 weighting combined with interface modification (25% of the maximum geodesic distance was
 211 set as the threshold to eliminate uncertainties caused by rough edges) method was used to

212 improve the curvature estimation by removing spurious values near the pore walls.

213 Wettability reflects the ability or tendency of one fluid to spread on the surface of a solid phase
 214 when there are other immiscible fluids in the system. It is usually characterized by the contact
 215 angle. In this work, an automated contact angle measurement algorithm (AlRatrouf et al., 2018a)
 216 was applied on segmented multiphase images to quantify geometric contact angle for both
 217 samples.



218

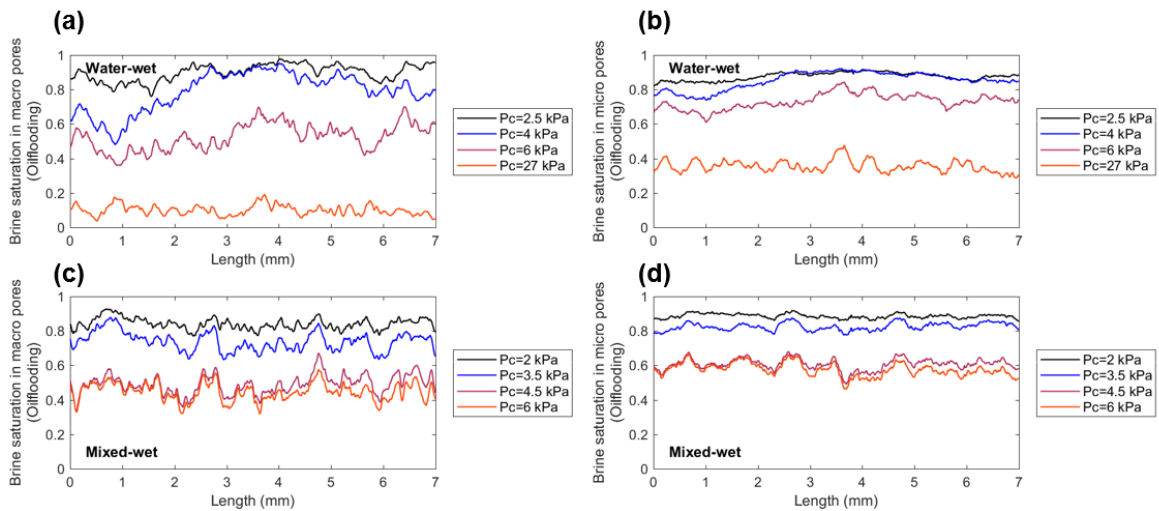
219 Figure 2. Two-dimensional cross-sections of filtered water-wet and mixed-wet samples. The top and bottom
 220 rows show the dry scan, the brine-saturated scan and the three phase segmentation for water-wet and mixed-
 221 wet cases respectively. The red, green and blue phases on segmentation map represent macropores,
 222 micropores and solid grain.

223 **3 Results and discussion**

224 In the following, we first describe the fluid distributions and quasi-static filling processes
 225 observed in the pore space based on the micro-CT images. Then, the wetting state and the
 226 network characteristics were analyzed to understand the underlying mechanisms of the
 227 complex fluid invasion behavior. Finally, the simulations on multi-scale PNMs were performed
 228 to link the pore-scale displacement to the fluid flow properties.

229 **3.1 Pore filling processes**

230 The brine saturation profiles along flow direction in both macro- and microporous regions at
 231 each oil flooding pressure step are shown in Figure 3. For the water-wet case, the brine
 232 saturation dropped dramatically with pressure increase, presenting a relatively uniform
 233 distribution at the highest pressure. At this point, there was a high brine saturation (41.29%) in
 234 the micropores. This was 5 times as high as the brine saturation in the macropores at the end
 235 of oil flooding. Under mixed-wet condition, the brine saturation in the micropores was also
 236 higher than in the macropores at all pressure steps, but the difference was smaller. This indicates
 237 weakly water-wet conditions in the microporosity.



238
 239 Figure 3. Average brine saturation distribution during the oil flooding, in slices perpendicular to the flow
 240 direction within macropores (left) and micropores (right) for water-wet and mixed-wet samples.

241 Figure 4 shows the evolution of the brine and oil clusters in macropores of the water-wet sample.

242 During the oil invasion sequence (Figure 4(a)), the oil found a main flow path and formed
243 several large clusters in the macro-pore space first, followed by occupying more and more
244 pores, while the brine phase gradually appeared more isolated. For a water-wet porous medium,
245 the typical displacement mechanism during oil flooding is a series of Haines jumps (Burst flow)
246 (Berg et al., 2013; Bultreys et al., 2015), i.e. a sudden rapid fluid interface movement through
247 a local constriction in the pore space, due to the dependence of the equilibrium capillary
248 pressure on the channel radius. As we aim to study the fluid distribution after a period of
249 equilibration at certain set capillary pressures, the images only reflect the fluid filling state after
250 many of these events. The branched structure connecting large pores together is consistent with
251 a capillary fingering type fluid distribution pattern that results from successive Haines jumps
252 (Blunt et al., 1992; Herring et al., 2014).

253 In the water-wet sample the waterflooding that followed the oilflooding increased the brine
254 saturation in the macroporous region from 8.5% to 22.7%, compared to that in the micropores
255 increasing from 50.7% to 79.3%. It is clear that in the resolved pore space (Figure 4(b)), brine
256 preferentially entered pores or throats with smaller sizes. In this process, brine films residing
257 in the corner or crevices of pores/throats at the end of oilflooding started to swell with the
258 decrease of capillary pressure, causing the interface configuration to become unstable when
259 films on opposing sides of the pore surface touched each other. On the micro-CT images, we
260 could clearly see a large amount of trapping due to snap-off, such as the example shown in
261 Figure 5.

262 For the mixed-wet case, on the other hand, the brine was displaced even at low pressures during
263 oil flooding. More small-volume brine clusters resided in the pore space, keeping the brine
264 connected, see Figure 6(a). The oil injection in the resolved pores of the mixed-wet sample was
265 different from the water-wet case: it tended to enter oil-wet or weakly water-wet pores at the
266 beginning of the displacement rather than filling the pores in order of their size (Scanziani et
267 al., 2020). The oil cluster volume distribution was therefore much smaller than in its water-wet
268 counterpart: e.g. the largest oil cluster volume at 6 kPa was 14% of the macropore volume for
269 water-wet (7.32 mm^3) and 2% of the macropore volume (0.59 mm^3) for mixed-wet. During

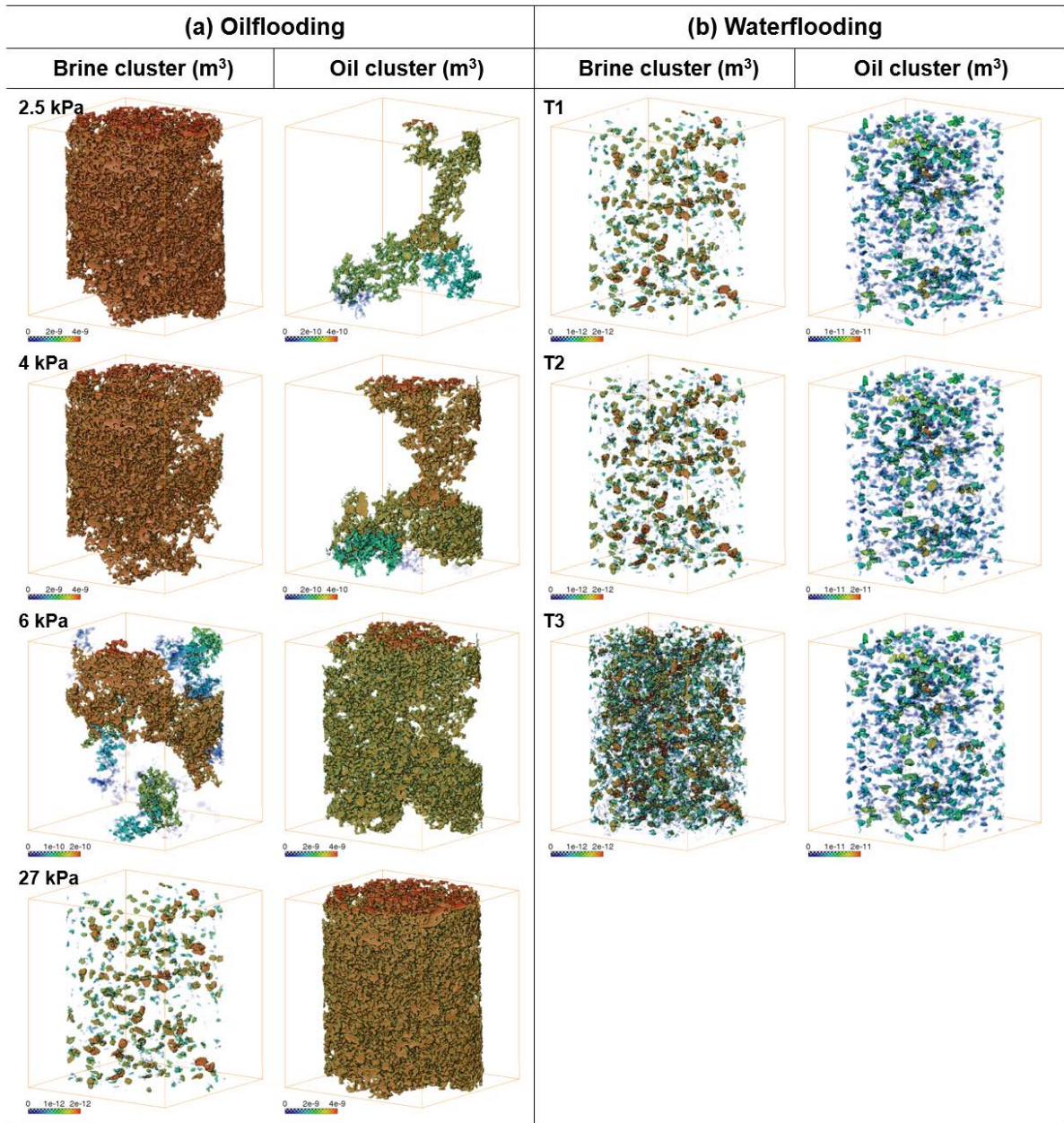
270 waterflooding of the mixed-wet sample, the brine saturation increased by only 3% in
271 macropores, and brine and oil cluster size distribution did not change significantly (Figure 6(b)).
272 While that in micropores showed a 5% increase. Compared to a sudden increase of brine
273 saturation in micropores of water-wet sample when the waterflooding started, that change in
274 micropores of mixed-wet case was much lower.

275 In comparison with the conventional pore filling phenomena for water-wet conditions, the fluid
276 flow mechanisms in the mixed-wet sample appeared to be more complex (Figure 7). The micro-
277 CT images showed that the fluid occupancy of most macropores made a step change from a
278 certain pressure step to the next. However, “gradually filling” events described by Mascini et
279 al. (2021) were also observed. This manifested itself in pores where terminal menisci appeared
280 to be quasi-stable everywhere while the three-phase contact line passed through it. Each such
281 pore was thus only partially invaded in between consecutive pressure steps. The menisci in
282 such pores remained present for multiple pressure steps at intervals of more than either 12 or 6
283 hours (respectively for oilflooding and waterflooding). The menisci curvatures gradually
284 increased or decreased with the imposed capillary pressure, reflecting the local capillary
285 pressure change. By detecting the interface movement at each pressure step during the
286 experiment, 3.4% of the macropores in oilflooding and 2.8% of the macropores in
287 waterflooding were found to reflect “gradually filling” phenomena, where these pores
288 accounted for 13% of the macropore volume. For convenience, we will refer to these as
289 “gradually filling pores” and to the others as “capillary instability pores” in the following
290 sections.

291 The morphology of the fluid menisci in gradually filling pores was markedly different from the
292 water-wet case, leading to three observations. The first observation is that the invading and
293 retreating of fluid in some pores can be approximated as a reversible process. As shown in pore
294 A (Figure 7(a)), the invading meniscus changed from a convex to a flat interface during oil
295 injection, and then bulged into oil again with the decrease of pressure, during which the
296 negative principal curvatures dominated over positive principal curvatures. The second
297 observation is a near flat front at the end of each oil flooding step in several pores (as shown in

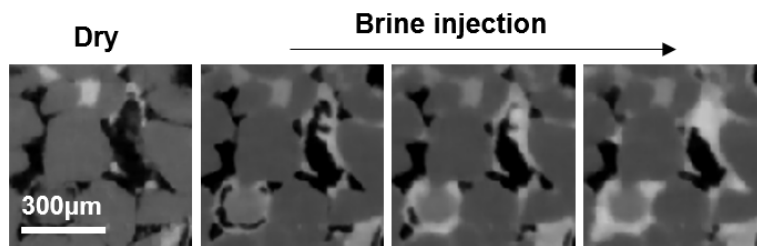
298 Figure 7(b)), indicating intermediate-wet conditions. The third observation is that the oil
299 flooding behavior in certain pores (Figure 7(c)) were distinct from that seen in the water-wet
300 case, where the large pores and throat were preferentially invaded by the oil phase, followed
301 by those with smaller sizes and finally microporosity, as these had high capillary invasion
302 pressures. To investigate this, we divided the microporosity near pore C in Figure 7(c) into 2
303 regions and tracked their grey value change. This showed that there was a significant decrease
304 of brine saturation in microporous region 2 compared to that in the microporous region 1.
305 Furthermore, the brine was completely displaced out of pore C while its saturation in
306 microporous region 1 was still high. This is likely due to the effect of wettability, which
307 impacted the order of filling here. This hypothesis will be further analyzed in the next section.

308 Overall, this section clearly shows that the fluid displacement behavior in both the 3D network
309 and in a single pore are markedly different in the untreated and treated rock samples. Further
310 analysis on wettability distribution and the neighboring network characteristics of pores in
311 treated sample will be presented in the following sections to point out the possible causes.



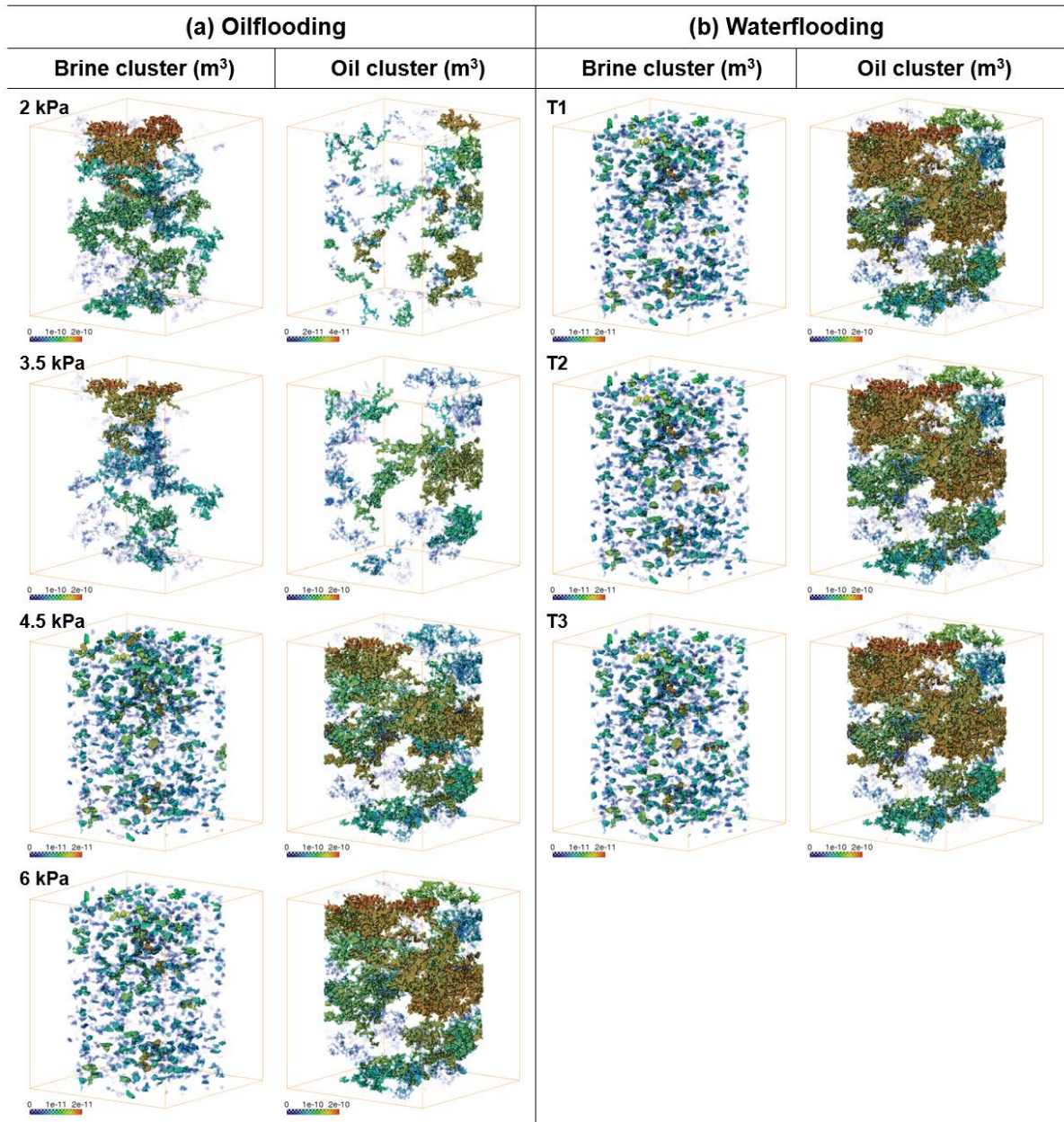
312

313 Figure 4. Fluid cluster changes in macropores of the water-wet sample during (a) oilflooding and (b)
 314 waterflooding. The color shows cluster volume (m³).



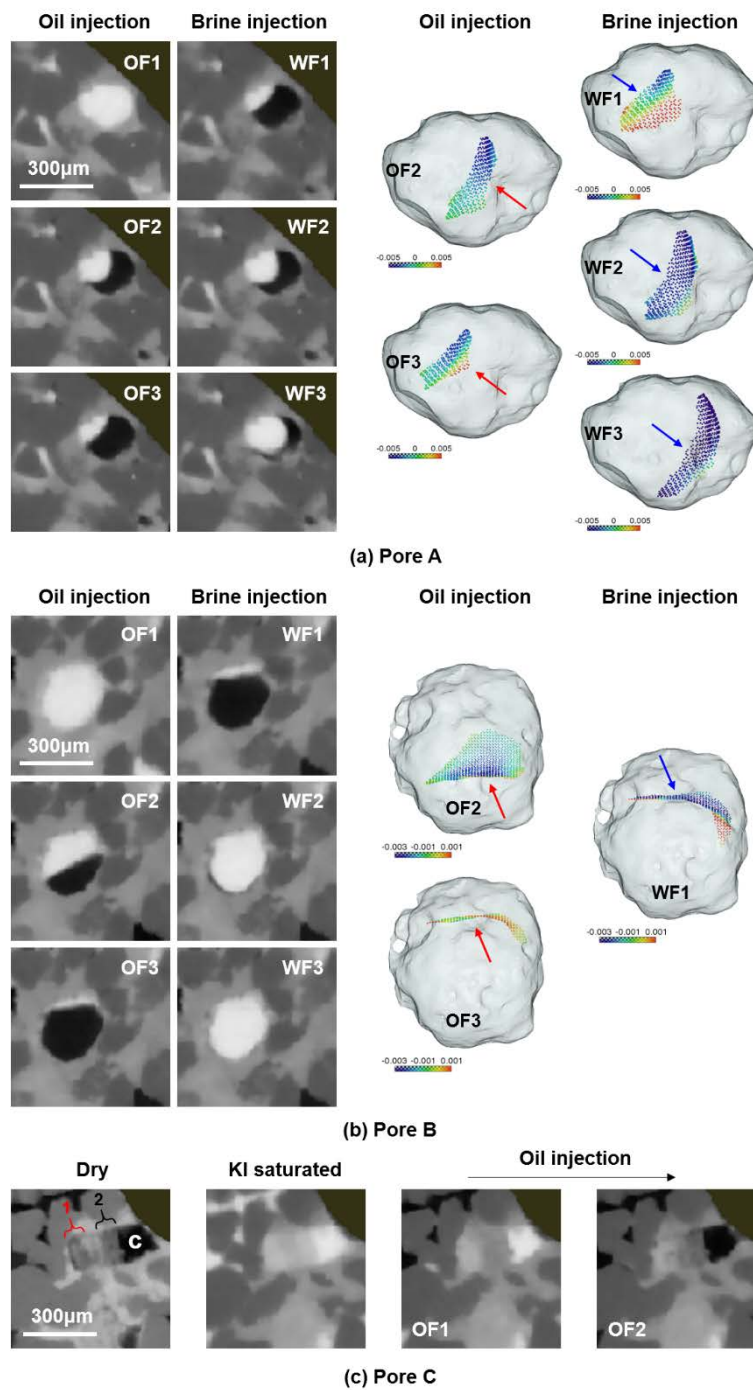
315

316 Figure 5. Example of two-dimensional views of oil phase trapping in pores under water-wet condition.



317

318 Figure 6. Fluid cluster changes in macropores of the mixed-wet sample during (a) oilflooding and (b)
 319 waterflooding. The color shows cluster volume (m³).



320

321 Figure 7. Examples of fluid invasion in pores of mixed-wet sample. (a) Oil-brine interfaces variation during
 322 oil and subsequent waterflooding in pore A. The figures on the left are 2D slices on X-Y plane. The figures
 323 on the right indicate the interfaces movement and the mean curvature distribution (colorful dots on interfaces)
 324 in 3D transparent pore space. The red and blue arrows show invasion direction of oil and brine phases
 325 respectively. (b) Movement of a flat shape interface on a 2D slice of pore B in oilflooding and waterflooding.
 326 (c) Invasion of oil phase from microporous region to a macropore C in oilflooding. The microporous phase

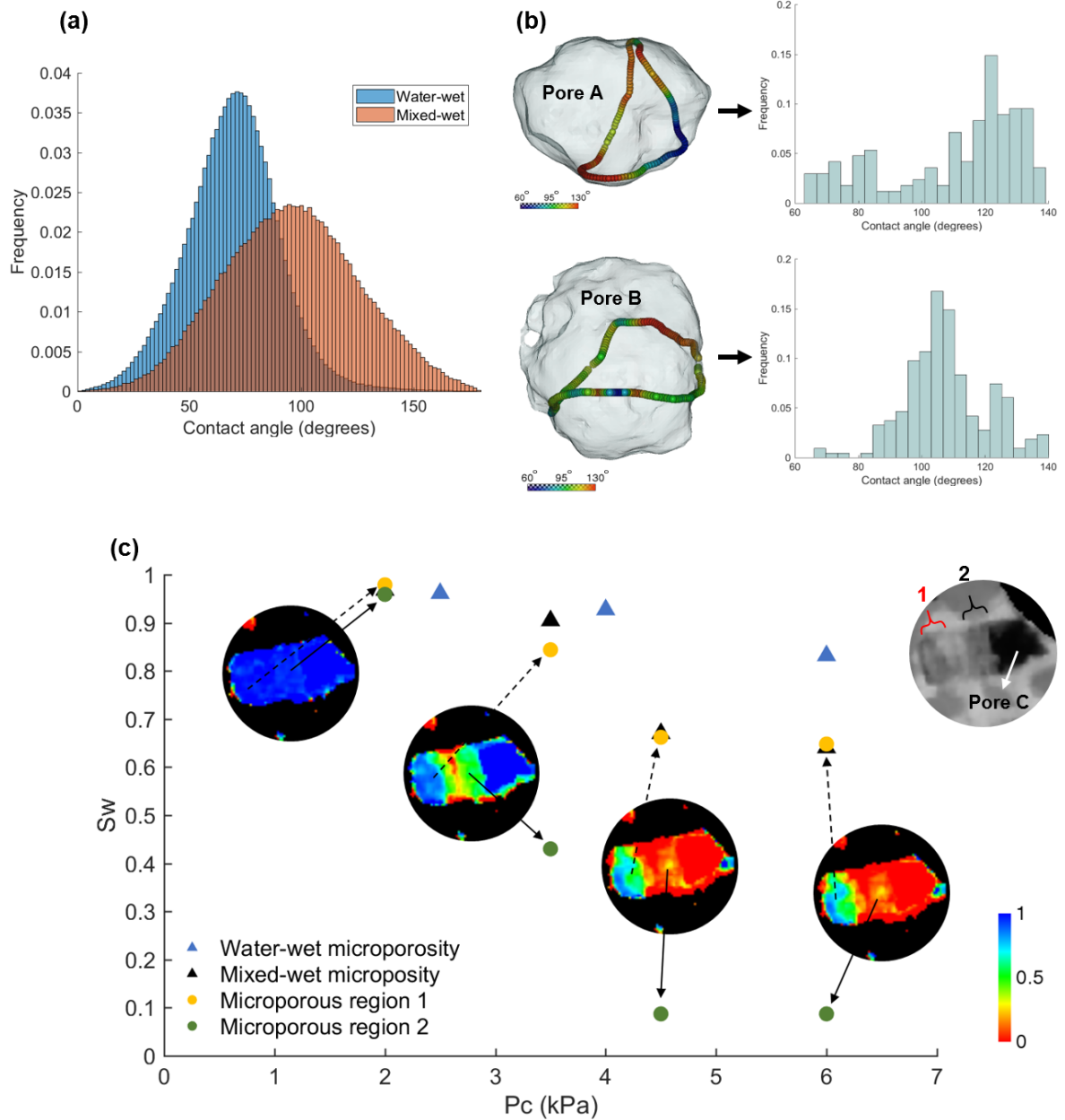
327 is divided into 2 regions according to their grey value change in oilflooding process.

328 **3.2 Wettability characterization**

329 For the resolved macropores, the wettability can be quantified by measuring the contact angle.
330 Figure (8) shows the results of geometric contact angles that were measured on full, segmented
331 micro-CT images at the last waterflooding step. The untreated and treated samples had a mean
332 contact angle of 69.23° and 95.50° respectively. The treated sample had a contact angle
333 distribution with a very broad range of values above and below 90° , implying a mixed-wet
334 state, while the contact angle distribution of the untreated sample implied weakly water-wet
335 conditions. Because the contact angle was calculated based on three-phase contact lines
336 extracted from the micro-CT images, the image resolution, selection of filtering methods and
337 segmentations affected measurements. In addition, the roughness of the pore surfaces in these
338 samples may also have been a key factor leading to wide range of contact angle, due to contact
339 angle pinning and hinging that is not picked up in static measurements (AlRatrou et al., 2017).
340 To investigate the wettability in gradually filling pore, Figure 8(b) presents the contact angle
341 distribution on pore A and pore B (micro-CT images are shown in Figure 7(a)) extracted from
342 the mixed-wet sample. Typically, the fluid meniscus remains concave (oil bulging into brine)
343 in water-wet pores, and is convex (brine bulging into oil) in oil-wet pores. However, the
344 wettability of the pore surfaces shown here was very heterogeneous, appearing to be partially
345 water-wet and partially oil-wet. The complex interaction between contact angle and pore space
346 geometry led to a variation in the interface morphology, resulting in both negative (i.e. oil
347 bulging into brine direction) and positive (i.e. brine bulging into oil direction) mean interfacial
348 curvatures occurring on the same fluid meniscus (see colored dots shown in 3D pores in Figure
349 7). Therefore, the movement of the invading phase in these mixed-wet pores might be inhibited
350 temporarily, but facilitated at the next time step, resulting in complex invasion behavior in the
351 pore space.

352 For the unresolved micropores, it is impossible to measure the contact angles directly, because
353 the fluid interfaces are not resolved. We therefore estimated the wetting state of the

354 microporosity by quantifying the evolution of its saturation based on the saturation maps from
355 differential imaging. Figure 8(b) shows an example of the application of this method on
356 microporous regions (the division of each region is shown in Figure 7 (c)) near pore C. The
357 decrease of brine saturation at each pressure step in the microporous regions of the water-wet
358 sample were very small, indicating that they were strongly water-wet: in this case, the filling
359 follows the order of pore size. However, the wettability of the microporosity in the mixed-wet
360 sample was more complicated, and it proved difficult to define a single wetting state obtained
361 from an average result to describe its characteristics. In the microporous regions that neighbour
362 pore C shown in Figure 7 (c), the saturation in region 2 decreased strongly, while that in region
363 1 was comparable to the average value of the whole microporous phase. Considering that the
364 saturation in pore C decreased to 0 already at a lower pressure (4.5 kPa), pore C is expected to
365 be more hydrophobic than microporous region 1. Therefore, we estimate that the latter is weakly
366 water-wet or weakly oil-wet and that microporous region 2 is strongly oil-wet. This means the
367 pore size was likely not the dominating factor for the filling sequence in the mixed-wet sample.



368

369 Figure 8. (a) Histogram of geometric contact angles measured on images after waterflooding under both
 370 conditions. (b) Example of contact angle distribution on pore A (top) and pore B (bottom) under mixed-wet
 371 condition and the corresponding distribution histograms. (c) Estimation of the wettability of the
 372 microporosity based on saturation change. Note that the saturation mentioned here is the average brine
 373 saturation in the microporous phase of the whole sample (triangle symbol) and in the specific microporous
 374 regions (circular symbol) in the oilflooding process. The four circular images show the saturation distribution
 375 map in microporous region 1, microporous region 2 and pore C at different pressure steps.

376 **3.3 Pore network characteristics**

377 **3.3.1 Multi-scale pore network extraction**

378 Extracting PNM from micro-CT images is an important tool to better understand the
379 characteristics of the pore space (Bultreys et al., 2015). The goal is to simplify some of the
380 network's complexity while its salient characteristics such as topology and geometry are
381 preserved. Because the samples used in this study presented multi-scale features with both
382 resolved macropores and unresolved micropores (i.e. pores below image resolution), and the
383 microporosity can play a key role in making the fluid flow behavior complex as stated in
384 previous section for the mixed-wet case, a state-of-the-art of the multi-scale modelling
385 technique (Ruspini et al., 2021) was used here. While direct multi-scale simulators are being
386 developed (Soulaine et al., 2016; Zhang et al., 2016), multi-scale PNM are currently still one
387 of the only models that allow to incorporate the microporosity characteristics on fairly large
388 image sizes for this type of complex samples. The extraction algorithm simplified the pore
389 geometry into 4 types of network elements: pore bodies and pore throats representing local
390 dilations and constrictions in the macroporous space, and Darcy nodes and links corresponding
391 to the (unresolved) microporosity phase treated as a continuum porous medium. The model
392 was constructed based on a 3D porosity map and a 3D rock type map (i.e. different flow zones
393 for the unresolved regions). Individual pore networks for the resolved pores and each of the
394 rock types were extracted first and then merged into a single multi-scale PNM by creating a
395 virtual link in the contact area between pores from different, neighboring zones. The porosity
396 map was used to determine the local porosity in each element, and each flow zone on the rock
397 type map was assigned different multiphase flow properties in the simulation process (the
398 details will be described in the next section).

399 The porosity distribution information is shown in Figure 9(a) and Table 1. The total porosity
400 was 18.11% and 15.14% for the water-wet and mixed-wet cases respectively. More than 30%
401 of the samples' volume fractions were made up of microporous voxels in both cases, and their
402 contribution to total porosity was equally important as the macropores. Therefore, the presence

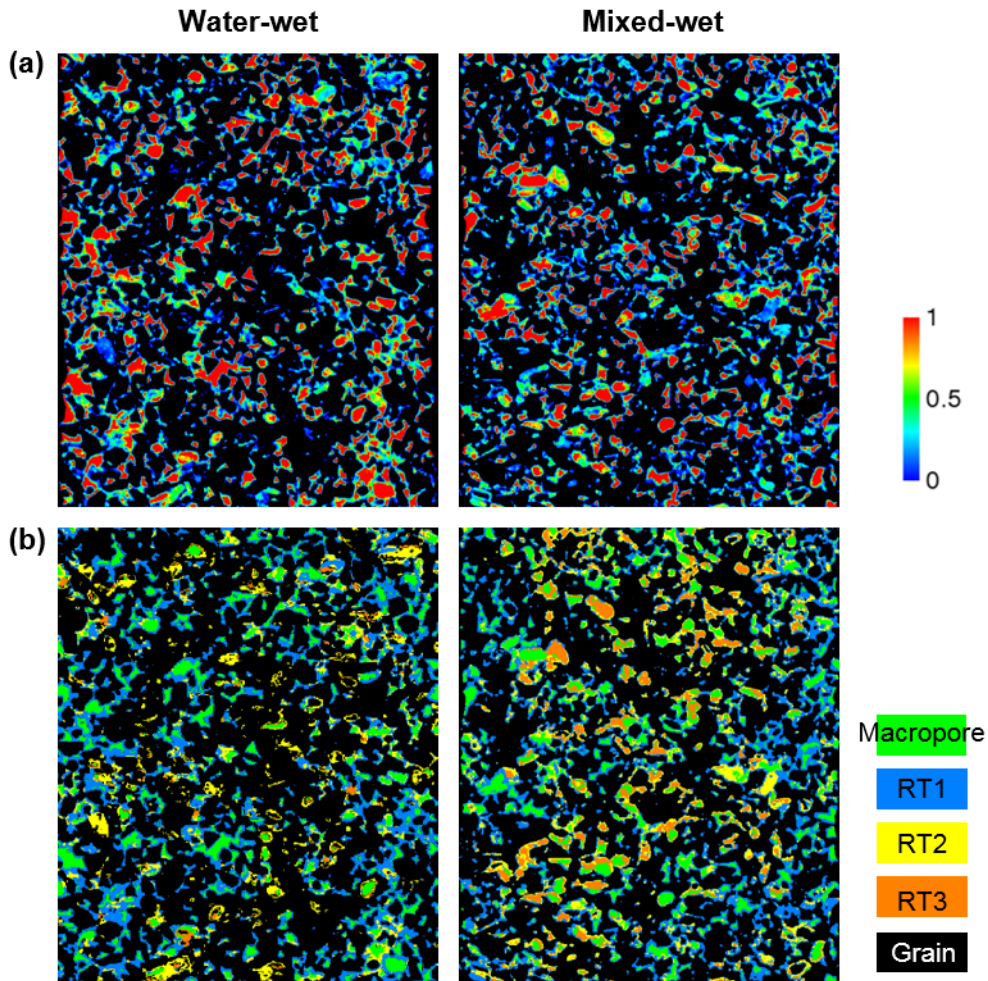
403 of microporosity increases the complexity of the pore space architecture, which may play an
404 important role in the multiphase flow. For the determination of the rock type map, we
405 introduced a method based on micro-CT images of obtained during capillary pressure
406 experiments in (Wang et al., 2022). The method was validated to be a promising approach in
407 decreasing the uncertainty of modelling, and was therefore used here. In this method, the
408 saturation and the corresponding capillary pressure of each microporous voxel in the sequence
409 of experimental images were first fitted using a Brooks-Corey-type Pc formulation (Brooks &
410 Corey, 1966) to obtain the invasion-capillary-pressure (Pct) distribution map of the sample.
411 Then, thresholds determined by k-means clustering were applied on the Pct map to divide the
412 microporous region into 3 rock types for both samples, see Figure 9(b).

413 It should be noted that in this study, the goal was to use the multi-scale PNM method to
414 understand the connectivity structure of the sample, and to try to estimate how it may influence
415 the flow behavior, rather than using it as a predictive simulation tool which aims to perfectly
416 match the experiments or predict properties.

417 **3.3.2 Network characteristics around gradually filling pores**

418 The properties of the two extracted PNMs are shown in Table 2. According to the network
419 model of the mixed-wet sample, we obtained the coordination number (CN) of 77, 139 and 90
420 for pore A, pore B and pore C respectively (micro-CT images are presented in Figure 7). The
421 CN reflects the amount of neighbours each pore has. The CN of pore B only consisted of Darcy
422 links, which means pore B was disconnected from all resolved pores and only connected by
423 unresolved pores. The average microporosity around pore B was 0.46. For pore A and pore C,
424 more than 97% of the CN were Darcy links (i.e. only 2 resolved throats around pore A and 3
425 resolved throats around pore C) with average microporosity of 0.46 and 0.57 respectively.
426 Especially in pore C, the average aspect ratio (the ratio of pore body size to pore throat size) of
427 the resolved throat configuration was very high (4.59). This likely explains the two crucial roles
428 of microporosity in gradually filling event: (i) slowing down the pore-scale invasion, (ii)
429 maintaining the connectivity of multiphase flow through complicated pore space, especially in

430 the isolated macropores. This may also be a possible reason why this invasion process was not
 431 reported in other relatively homogeneous mixed-wet media (Scanziani et al., 2020).



432
 433 Figure 9. (a) Porosity distribution maps for water-wet (left) and mixed-wet samples (right). (b) Rock type
 434 maps for water-wet (left) and mixed-wet samples (right). On the rock type maps, the macropore region and
 435 solid grain are shown in green color and black color respectively. The RT1, RT2 and RT3 refer to 3
 436 microporous regions with invasion capillary pressures from low to high values.

437 Table 1 Porosity and volume fraction of each phase in the samples.

Sample	Phase	Average porosity	Volume fraction	Contribution	Total porosity
	Macropore	1	0.0954	0.0954	
Water-wet	Micropore	0.2756	0.3109	0.0857	0.1811
	Solid grain	0	0.5937	0	

	Macropore	1	0.0741	0.0741	
Mixed-wet	Micropore	0.2554	0.3027	0.0773	0.1514
	Solid grain	0	0.6232	0	

438

Table 2 Properties of the multi-scale PNMs for two samples.

Properties	Water-wet	Mixed-wet
Resolved Nodes	53393	57468
Resolved Links	32372	20606
Darcy Nodes	427392	526917
Darcy Links	2352556	2902592
Average CN (Resolved Nodes)	12.15	11.76
Average CN (Darcy Nodes)	9.63	9.80
Average macropore radius (μm)	15.13	12

439

3.4 Influence of gradually filling event on flow properties

440

Quasi-static PNM (such as the one used here) by definition do not allow to simulate the dynamics of multiphase flow, for example the slow movement of the fluid menisci in the pores.

441

442

These models assume that the capillary forces play a dominant role in controlling the invasion order of fluids in the pore space, so that the macropores change fluid occupancy in a single

443

444

pressure or saturation step, while the influence of viscous forces on the displacement sequence

445

are entirely neglected. Dynamic models, on the other hand, are computationally much more

446

complex, and are therefore difficult to use in the complex samples investigated here. To

447

nevertheless study the sensitivity of flow properties to gradually filling pores, we established

448

two quasi-static models with different network structures for the mixed-wet sample. Model A

449

was already introduced in section 3.3.1; this was a conventional multi-scale PNM without

450

considering “gradually filling” behavior in certain macropores. It included 1 macropore phase,

451

3 types of microporous flow zones and 1 solid grain phase. In model B, gradually filling

452

macropores were treated as “microporosity”: we applied the aforementioned “rock typing”

453

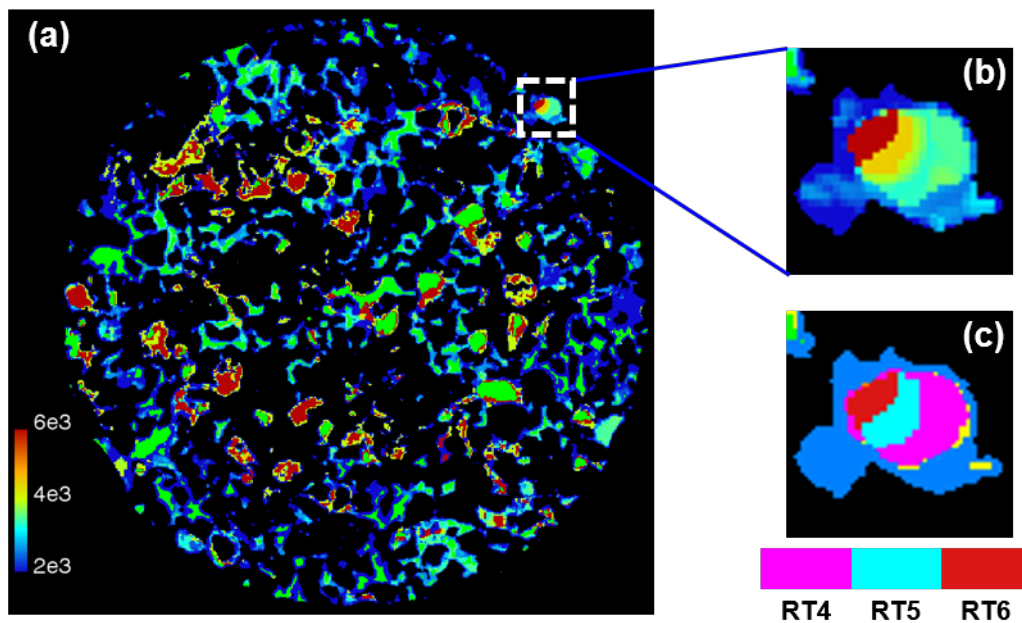
method on them to divide a single macropore into different flow zones (Figure 10). It should

454 be noted that the goal was to make the effective behavior of the quasi-static PNM similar to the
455 experiment without including the detailed physics of the process. To differentiate the fluid
456 invasion mechanism in microporosity and in gradually filling macropores in the model, the
457 properties for gradually filling regions were user-defined so as to obtain a gradual filling here.
458 The model can only be expected to give a coarse estimate of what the inclusion of this behavior
459 on the simulation would be, rather than provide accurate ab-initio prediction results. As shown
460 in Figure 10(c), each flow zone was assigned an invasion capillary pressure according to the
461 segmentation thresholds, which means the zone would be invaded by oil phase when the
462 injection pressure reached this pressure. This way, we simulated the effect of the “gradual
463 filling” process in macropores. This model contains 1 macropore phase, 3 microporous flow
464 zones, 3 gradually filling zones and 1 solid grain phase.

465 The input petrophysical properties for each rock type included capillary pressure curve (Pc-
466 curve), relative permeability (kr-curve) and permeability. The input Pc-curve was completely
467 based on our experimental data (for more details regarding this procedure, we refer to our
468 previous publication (Wang et al., 2022)). The kr-curve was obtained based on the Brooks-
469 Corey model. A power correlation $k = a \cdot \varphi^b$ was used to determine the permeability for each
470 node in the model, where we fixed the parameter b and tuned the parameter a until the output
471 Pc-curve matched the experimental data (Ruspini et al., 2021). A Gaussian distribution of
472 contact angles were assigned with values between 10° and 160° to mimic the complex wetting
473 state of the sample. All the aforementioned parameters were the same for two models, except
474 that in model B, the permeability of the gradually filling pores was assigned from a very small
475 value (i.e. case 1 in Figure 11(a)) to a very large value (i.e. case 2 in Figure 11(a)). This is
476 meant to perform a sensitivity study on the importance of these pores on the flow, by mimicking
477 that these pores are open for flow or that their contribution to the flow is negligible. In this test,
478 we only simulated the oil flooding process.

479 The results showed that the absolute permeability of model A was 29.86 mD. For model B, as
480 shown in Figure 11(a), the absolute permeability of the sample remained approximately stable
481 when the permeability of gradually filling pores was set lower than 1 mD or higher than 100

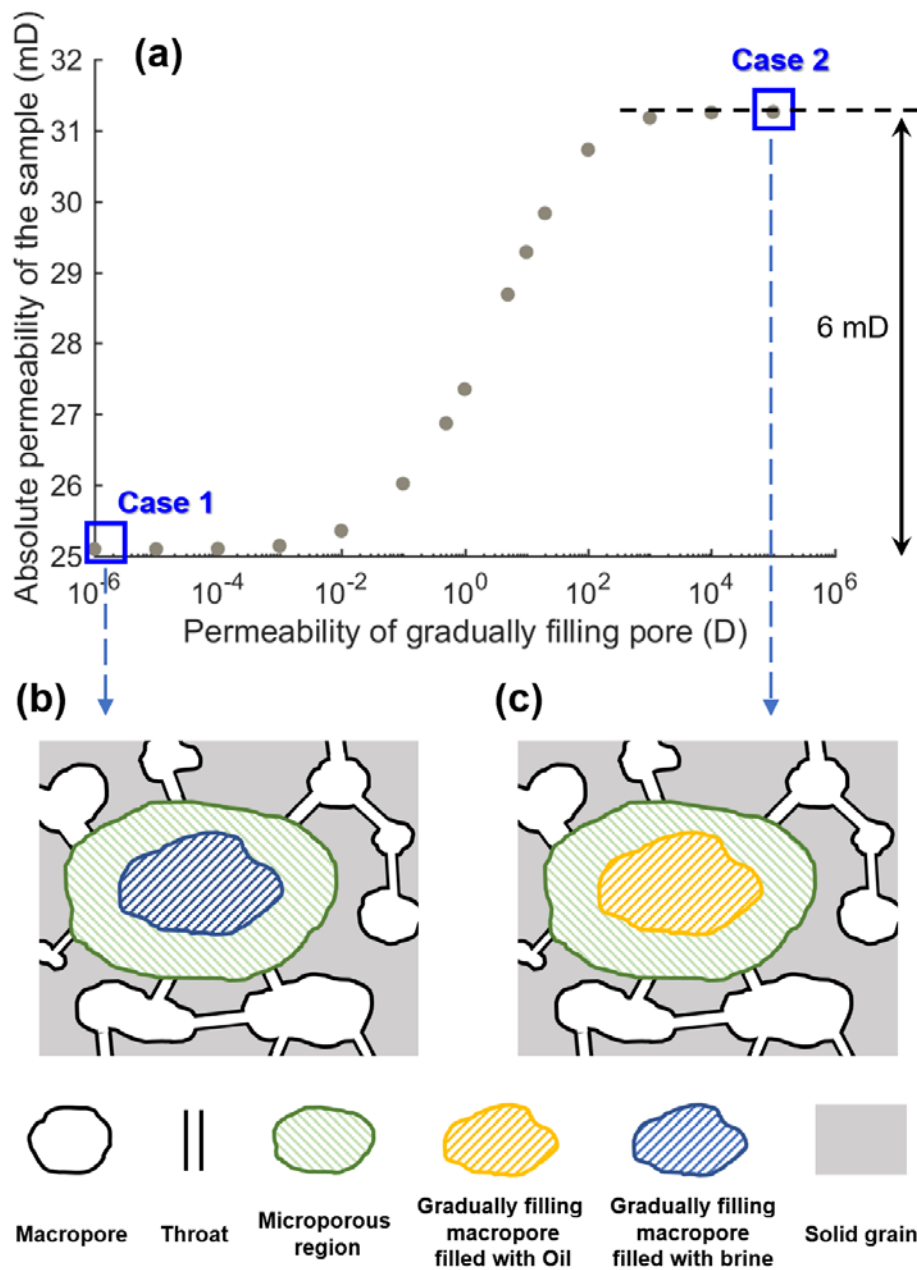
482 D, presenting an S-shape in the semilog coordinates. The total effect of gradually filling pores
 483 on the permeability of the sample was therefore 6 mD, approximately 19% of the maximum
 484 value. Figure 12 shows the comparison of the P_c -curves and the k_r -curves simulated by
 485 different models. All P_c -curves had a good match with the experimental data and there is very
 486 little difference between the two models. The former was due to the fact that the input P_c -curve
 487 for Darcy pores were scaled with their porosity and permeability. The k_r -curves indicated that
 488 gradually filling pores may affect the relative permeability of the brine phase, but that their
 489 effect is small. As depicted in Figure 11(b) and (c), the gradually filling pores were surrounded
 490 by micropores, which provided their connection with the other macropores and throats. During
 491 the oil flooding process, the case where the gradually filling pores had very low permeability
 492 (case 1) simulated that these pores were fully occupied by brine and the oil could not enter.
 493 This provided more flow paths for the brine, thus the brine relative permeability was higher. If
 494 their permeability was very high (case 2), the invading oil would pass through these pores
 495 easily, causing the brine to lose connected pathways, causing the brine relative permeability
 496 curve to decrease. As the model used in this study did not take into account the rate effects on
 497 the relative permeability, further developments in dynamic simulations are needed to fully
 498 investigate the results presented here.



499

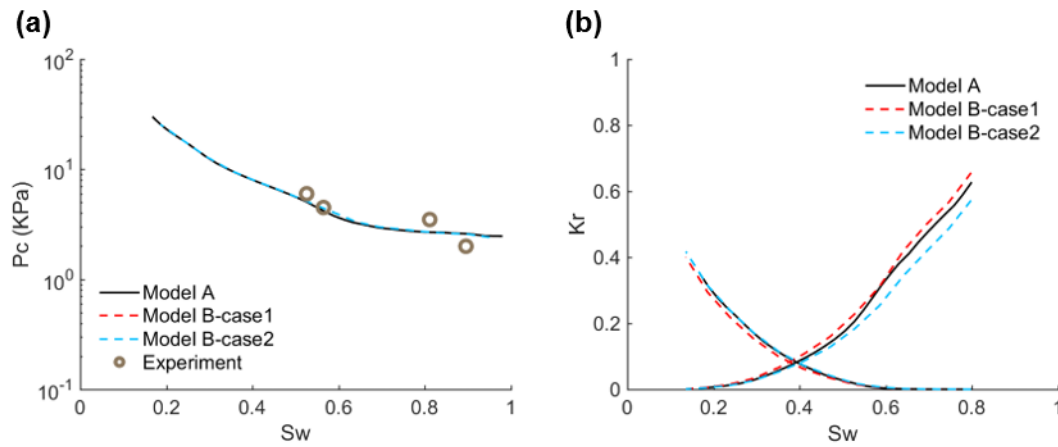
500 Figure 10. (a) A slice of invasion capillary pressure distribution on X-Y plane of the mixed-wet sample. The

501 “capillary instability pores” are marked in green. (b) A zoom in view of “pressure distribution” in pore A.
 502 Note that the pressure in “gradually filling pores” does not have the same meaning as in the microporosity.
 503 It only represents the moving sequence of fluid-fluid interfaces in macropores, i.e. “low pressure region” is
 504 invaded first, followed by the “high pressure region”. (c) An example of “rock typing” results for pore A in
 505 model B. The segmentation of RT1-RT3 in model B is the same as model A, see Figure 9b. The RT4, RT5
 506 and RT6 represent gradually filling zones.



507
 508 Figure 11. (a) Simulation results of the input permeability value for gradually filling pores and the absolute
 509 permeability of the sample. (b) Diagram of the gradually filling pore blocked by brine at very low

510 permeability condition during two phase flow. (c) Diagram of the gradually filling pore blocked by oil at
 511 very high permeability condition during two phase flow.



512
 513 Figure 12. Results of oilflooding simulations. (a) Comparison of capillary pressure curves from the two
 514 models and the experiment. (b) Relative permeability curves of the two models.

515 4 Conclusions

516 We present an experimental workflow based on X-ray micro-CT to study fluid invasion
 517 behavior in heterogeneous rocks with different wettability via quasi-static oil- and
 518 waterflooding. We observed typical oil phase trapping in macropores of a water-wet sample
 519 during waterflooding, while in its mixed-wet counterpart, some macropores were observed to
 520 be filled gradually compared to others that were completely occupied by invasion fluid in a
 521 single pressure step. This occurred during both oil flooding and water flooding. To understand
 522 why and how the gradually filling pores behave under mixed-wet conditions, we analyzed the
 523 wettability and pore network characteristics. We introduced a new approach to perform a
 524 sensitivity study of the impact of the slow displacements on the multiphase flow properties,
 525 using a state-of-the-art multi-scale PNM.

526 We quantified the wettability of macropores in each sample by measuring the contact angle on
 527 multiphase micro-CT images, and found that the gradually filling pores in mixed-wet case had
 528 a high degree of wetting heterogeneity on their pore walls, presenting partially water-wet and
 529 partially oil-wet regions. This may alternately inhibit and facilitate the movement of invading

530 phase at different times during displacement, resulting in complex invasion behavior in the
531 pore space. In this study, the wettability of the microporosity was evaluated by quantifying its
532 saturation, shedding new light on the slow displacements first characterized by Mascini et al.
533 (2021). The results indicated that the mixed wettability impacted the pore filling sequence and
534 increased the complexity of multiphase flow. To mimic the slow movement of menisci in the
535 model and the importance of this factor in flow simulation, we constructed two multi-scale
536 PNMs. One was a conventional model with macropore phase, solid grain phase and 3
537 microporous flow zones classified by fitting saturation and capillary pressure of each voxel. It
538 showed that the gradually filling pores presented a high CN, and more than 97% of the CN was
539 contributed by micro-elements. This proved that the microporosity provided the “supply chain”
540 for the gradually filling pores, which on one hand slowed down the pore-scale invasion and on
541 the other hand maintained the connectivity of fluids in those macropores. The second model
542 had the same segmentation of “capillary instability pores”, microporous phase and solid grain
543 as the previous model, except that the gradually filling macropores were divided into distinct
544 invasion zones to mimic their slow filling. The results showed that the total effect of gradually
545 filling pores on the permeability of the sample was 6 mD (approximately 19% of the maximum
546 value), but that their influence on the relative permeability may be smaller. This needs to be
547 further investigated with dynamic simulations to provide a definite answer.

548 In general, our work demonstrates that the fluid filling process in heterogeneous porous media
549 is strongly correlated with wetting state and multi-scale pore space structures. The
550 methodologies presented here can be extended to other geological materials for better
551 modelling and simulation of multiphase flow in porous media. Further work is needed to clarify
552 how the mixed wettability distribution obtained with the chemical wettability alteration method
553 used here compares to specific cases in reservoirs and aquifers, including “ageing” by contact
554 with crude oil or non-aqueous phase liquids. This is particularly the case for situations where
555 the alteration takes place on surfaces exposed to oil but not on those exposed to water (Kovscek
556 et al., 1993).

557 **Acknowledgments**

558 Shan Wang would like to acknowledge the China Scholarship Council (CSC Grant
559 201906440157) for PhD support. Tom Bultreys is a postdoctoral fellow of the Research
560 Foundation–Flanders (FWO) and acknowledges its support under grant 12X0919N. The
561 special research fund of the Ghent University (BOF-UGent) is acknowledged for the financial
562 support to the UGCT Centre of Expertise (BOF.EXP.2017.0007). Leonardo Ruspini would like
563 to acknowledge “Norges Forskningrådet” (grant number 296093) for partial support to this
564 research. Arjen Mascini acknowledges funding from the Research Foundation–Flanders (FWO,
565 project G051418N).

566 **References**

567 Al-Futaisi, A., & Patzek, T. W. (2004). Secondary imbibition in NAPL-invaded mixed-wet
568 sediments. *Journal of Contaminant Hydrology*, 74(1–4), 61–81.

569 Alhammadi, A. M., Gao, Y., Akai, T., Blunt, M. J., & Bijeljic, B. (2020). Pore-scale X-ray
570 imaging with measurement of relative permeability, capillary pressure and oil recovery
571 in a mixed-wet micro-porous carbonate reservoir rock. *Fuel*, 268(January), 117018.
572 <https://doi.org/10.1016/j.fuel.2020.117018>

573 AlRatrouf, A., Raeini, A. Q., Bijeljic, B., & Blunt, M. J. (2017). Automatic measurement of
574 contact angle in pore-space images. *Advances in Water Resources*, 109, 158–169.
575 <https://doi.org/10.1016/j.advwatres.2017.07.018>

576 AlRatrouf, A., Blunt, M. J., & Bijeljic, B. (2018a). Spatial Correlation of Contact Angle and
577 Curvature in Pore-Space Images. *Water Resources Research*, 54(9), 6133–6152.
578 <https://doi.org/10.1029/2017WR022124>

579 AlRatrouf, A., Blunt, M. J., & Bijeljic, B. (2018b). Wettability in complex porous materials,
580 the mixed-wet state, and its relationship to surface roughness. *Proceedings of the*
581 *National Academy of Sciences of the United States of America*, 115(36), 8901–8906.
582 <https://doi.org/10.1073/pnas.1803734115>

- 583 Andrew, M., Bijeljic, B., & Blunt, M. J. (2014). Pore-scale contact angle measurements at
584 reservoir conditions using X-ray microtomography. *Advances in Water Resources*, 68,
585 24–31. <https://doi.org/10.1016/j.advwatres.2014.02.014>
- 586 Berg, S., Ott, H., Klapp, S. A., Schwing, A., Neiteler, R., Brussee, N., & Makurat, A. (2013).
587 Real-time 3D imaging of Haines jumps in porous media flow, *110*(10), 3755–3759.
588 <https://doi.org/10.1073/pnas.1221373110>
- 589 Berg, S., Ott, H., Klapp, S. A., Schwing, A., Neiteler, R., Brussee, N., Makurat, A., et al.
590 (2013). Real-time 3D imaging of Haines jumps in porous media flow. *Proceedings of*
591 *the National Academy of Sciences*, *110*(10), 3755–3759.
- 592 Blunt, M., King, M. J., & Scher, H. (1992). Simulation and theory of two-phase flow in
593 porous media. *Physical Review A*, *46*(12), 7680.
- 594 Blunt, M. J., Lin, Q., Akai, T., & Bijeljic, B. (2019). A thermodynamically consistent
595 characterization of wettability in porous media using high-resolution imaging. *Journal*
596 *of Colloid and Interface Science*, *552*, 59–65. <https://doi.org/10.1016/j.jcis.2019.05.026>
- 597 Brooks, R. H., & Corey, A. T. (1966). Properties of porous media affecting fluid flow.
598 *Journal of the Irrigation and Drainage Division*, *92*(2), 61–88.
- 599 Buades, A., Coll, B., & Morel, J.-M. (2008). Nonlocal image and movie denoising.
600 *International Journal of Computer Vision*, *76*(2), 123–139.
- 601 Buckley, J. S., Liu, Y., & Monsterleet, S. (1998). Mechanisms of Wetting Alteration by
602 Crude Oils. *SPE Journal*, *3*(1), 54–61. <https://doi.org/10.2118/37230-PA>
- 603 Bultreys, T., Van Hoorebeke, L., & Cnudde, V. (2015). Multi-scale, micro-computed
604 tomography-based pore network models to simulate drainage in heterogeneous rocks.
605 *Advances in Water Resources*, *78*, 36–49.
606 <https://doi.org/10.1016/j.advwatres.2015.02.003>
- 607 Bultreys, T., Boone, M. A., Boone, M. N., De Schryver, T., Masschaele, B., Van Loo, D., et
608 al. (2015). Real-time visualization of Haines jumps in sandstone with laboratory-based

- 609 microcomputed tomography. *Water Resources Research*, 51(10), 8668–8676.
610 <https://doi.org/10.1002/2015WR017502>
- 611 Bultreys, T., Boone, M. A., Boone, M. N., De Schryver, T., Masschaele, B., Van Hoorebeke,
612 L., & Cnudde, V. (2016). Fast laboratory-based micro-computed tomography for pore-
613 scale research: Illustrative experiments and perspectives on the future. *Advances in*
614 *Water Resources*, 95, 341–351. <https://doi.org/10.1016/j.advwatres.2015.05.012>
- 615 Bultreys, T., Lin, Q., Gao, Y., Raeini, A. Q., Alratrout, A., Bijeljic, B., & Blunt, M. J. (2018).
616 Validation of model predictions of pore-scale fluid distributions during two-phase flow.
617 *Physical Review E*, 97(5). <https://doi.org/10.1103/PhysRevE.97.053104>
- 618 Burger, W., & Burge, M. J. (2010). *Principles of digital image processing: core algorithms*.
619 Springer Science & Business Media.
- 620 Chen, Y., Jha, N. K., Lebedev, M., An, S., Xie, Q., & Niasar, V. J. (2021). Integral effects of
621 initial fluids configuration and wettability alteration on remaining saturation:
622 characterization with X-ray micro-computed tomography. *Fuel*, 306, 121717.
- 623 Datta, S. S., Ramakrishnan, T. S., & Weitz, D. A. (2014). Mobilization of a trapped non-
624 wetting fluid from a three-dimensional porous medium. *Physics of Fluids*, 26(2), 22002.
625 <https://doi.org/10.1063/1.4866641>
- 626 Dierick, M., Van Loo, D., Masschaele, B., Van Den Bulcke, J., Van Acker, J., Cnudde, V., &
627 Van Hoorebeke, L. (2014). Recent micro-CT scanner developments at UGCT. *Nuclear*
628 *Instruments and Methods in Physics Research, Section B: Beam Interactions with*
629 *Materials and Atoms*, 324, 35–40. <https://doi.org/10.1016/j.nimb.2013.10.051>
- 630 Gao, Y., Qaseminejad Raeini, A., Blunt, M. J., & Bijeljic, B. (2019). Pore occupancy, relative
631 permeability and flow intermittency measurements using X-ray micro-tomography in a
632 complex carbonate. *Advances in Water Resources*, 129(April), 56–69.
633 <https://doi.org/10.1016/j.advwatres.2019.04.007>
- 634 Gao, Y., Raeini, A. Q., Selem, A. M., Bondino, I., Blunt, M. J., & Bijeljic, B. (2020). Pore-

- 635 scale imaging with measurement of relative permeability and capillary pressure on the
636 same reservoir sandstone sample under water-wet and mixed-wet conditions. *Advances*
637 *in Water Resources*, 146(July). <https://doi.org/10.1016/j.advwatres.2020.103786>
- 638 Garfi, G., John, C. M., Lin, Q., Berg, S., & Krevor, S. (2020). Fluid Surface Coverage
639 Showing the Controls of Rock Mineralogy on the Wetting State. *Geophysical Research*
640 *Letters*, 47(8), e2019GL086380. <https://doi.org/10.1029/2019GL086380>
- 641 Garing, C., de Chalendar, J. A., Voltolini, M., Ajo-Franklin, J. B., & Benson, S. M. (2017).
642 Pore-scale capillary pressure analysis using multi-scale X-ray micromotography.
643 *Advances in Water Resources*, 104, 223–241.
644 <https://doi.org/10.1016/j.advwatres.2017.04.006>
- 645 Herring, A. L., Andersson, L., Newell, D. L., Carey, J. W., & Wildenschild, D. (2014). Pore-
646 scale observations of supercritical CO₂ drainage in Bentheimer sandstone by
647 synchrotron x-ray imaging. *International Journal of Greenhouse Gas Control*, 25, 93–
648 101.
- 649 Herring, A. L., Middleton, J., Walsh, R., Kingston, A., & Sheppard, A. (2017). Flow rate
650 impacts on capillary pressure and interface curvature of connected and disconnected
651 fluid phases during multiphase flow in sandstone. *Advances in Water Resources*, 107,
652 460–469. <https://doi.org/10.1016/j.advwatres.2017.05.011>
- 653 Iglauer, S., Paluszny, A., Pentland, C. H., & Blunt, M. J. (2011). Residual CO₂ imaged with
654 X-ray micro-tomography. *Geophysical Research Letters*, 38(21).
655 <https://doi.org/10.1029/2011GL049680>
- 656 Kalhor, K., Ghasemizadeh, R., Rajic, L., & Alshwabkeh, A. (2019). Assessment of
657 groundwater quality and remediation in karst aquifers: A review. *Groundwater for*
658 *Sustainable Development*, 8, 104–121. <https://doi.org/10.1016/j.gsd.2018.10.004>
- 659 Klise, K. A., Moriarty, D., Yoon, H., & Karpyn, Z. (2016). Automated contact angle
660 estimation for three-dimensional X-ray microtomography data. *Advances in Water*
661 *Resources*, 95, 152–160. <https://doi.org/10.1016/j.advwatres.2015.11.006>

- 662 Kovscek, A. R., Wong, H., & Radke, C. J. (1993). A pore-level scenario for the development
663 of mixed wettability in oil reservoirs. *AIChE Journal*, 39(6), 1072–1085.
- 664 Li, T., Schlüter, S., Dragila, M. I., & Wildenschild, D. (2018). An improved method for
665 estimating capillary pressure from 3D microtomography images and its application to
666 the study of disconnected nonwetting phase. *Advances in Water Resources*, 114, 249–
667 260. <https://doi.org/10.1016/j.advwatres.2018.02.012>
- 668 Lin, Q., Al-Khulaifi, Y., Blunt, M. J., & Bijeljic, B. (2016). Quantification of sub-resolution
669 porosity in carbonate rocks by applying high-salinity contrast brine using X-ray
670 microtomography differential imaging. *Advances in Water Resources*, 96, 306–322.
671 <https://doi.org/10.1016/j.advwatres.2016.08.002>
- 672 Lin, Q., Akai, T., Blunt, M. J., Bijeljic, B., Iwama, H., Takabayashi, K., et al. (2021). Pore-
673 scale imaging of asphaltene-induced pore clogging in carbonate rocks. *Fuel*, 283,
674 118871.
- 675 Lin, Q., Bijeljic, B., Foroughi, S., Berg, S., & Blunt, M. J. (2021). Pore-scale imaging of
676 displacement patterns in an altered-wettability carbonate. *Chemical Engineering
677 Science*, 235, 116464. <https://doi.org/10.1016/j.ces.2021.116464>
- 678 Mascini, A., Cnudde, V., & Bultreys, T. (2020). Event-based contact angle measurements
679 inside porous media using time-resolved micro-computed tomography. *Journal of
680 Colloid and Interface Science*, 572, 354–363. <https://doi.org/10.1016/j.jcis.2020.03.099>
- 681 Mascini, A., Boone, M., Van Offenwert, S., Wang, S., Cnudde, V., & Bultreys, T. (2021).
682 Fluid Invasion Dynamics in Porous Media With Complex Wettability and Connectivity.
683 *Geophysical Research Letters*, 48(22), 1–10. <https://doi.org/10.1029/2021GL095185>
- 684 Molenaar, N. (1998). Origin of low-permeability calcite-cemented lenses in shallow marine
685 sandstones and CaCO₃ cementation mechanisms: An example from the Lower Jurassic
686 Luxemburg Sandstone, Luxemburg. *Carbonate Cementation in Sandstones: Distribution
687 Patterns and Geochemical Evolution*, 193–211.

- 688 Morrow, N. R. (1990). Wettability and its effect on oil recovery. *JPT, Journal of Petroleum*
689 *Technology*, 42(12), 1476–1484. <https://doi.org/10.2118/21621-PA>
- 690 Offenwert, S. Van. (2019). Pore - Scale Visualization and Quanti fi cation of Transient
691 Solute Transport Using Fast Microcomputed Tomography *Water Resources Research*,
692 9279–9291. <https://doi.org/10.1029/2019WR025880>
- 693 Panfilov, M. (2010). Underground Storage of Hydrogen: In Situ Self-Organisation and
694 Methane Generation. *Transport in Porous Media*, 85(3), 841–865.
695 <https://doi.org/10.1007/s11242-010-9595-7>
- 696 Reynolds, C. A., Menke, H., Andrew, M., Blunt, M. J., & Krevor, S. (2017). Dynamic fluid
697 connectivity during steady-state multiphase flow in a sandstone. *Proceedings of the*
698 *National Academy of Sciences of the United States of America*, 114(31), 8187–8192.
699 <https://doi.org/10.1073/pnas.1702834114>
- 700 Rücker, M., Berg, S., Armstrong, R. T., Georgiadis, A., Ott, H., Schwing, A., et al. (2015).
701 From connected pathway flow to ganglion dynamics. *Geophysical Research Letters*,
702 42(10), 3888–3894. <https://doi.org/10.1002/2015GL064007>
- 703 Ruspini, L. C., Øren, P. E., Berg, S., Masalmeh, S., Bultreys, T., Taberner, C., et al. (2021).
704 Multiscale Digital Rock Analysis for Complex Rocks. *Transport in Porous Media*,
705 139(2), 301–325. <https://doi.org/10.1007/s11242-021-01667-2>
- 706 Scanziani, A., Singh, K., Blunt, M. J., & Guadagnini, A. (2017). Automatic method for
707 estimation of in situ effective contact angle from X-ray micro tomography images of
708 two-phase flow in porous media. *Journal of Colloid and Interface Science*, 496, 51–59.
709 <https://doi.org/10.1016/j.jcis.2017.02.005>
- 710 Scanziani, A., Lin, Q., Alhosani, A., Blunt, M. J., & Bijeljic, B. (2020). Dynamics of fluid
711 displacement in mixed-wet porous media. *Proceedings of the Royal Society A*,
712 476(2240), 20200040.
- 713 Shukla, R., Ranjith, P., Haque, A., & Choi, X. (2010). A review of studies on CO₂

- 714 sequestration and caprock integrity. *Fuel*, 89(10), 2651–2664.
715 <https://doi.org/10.1016/j.fuel.2010.05.012>
- 716 Singh, K., Bultreys, T., Raeini, A. Q., Shams, M., & Blunt, M. J. (2022). New type of pore-
717 snap-off and displacement correlations in imbibition. *Journal of Colloid and Interface*
718 *Science*, 609, 384–392. <https://doi.org/10.1016/j.jcis.2021.11.109>
- 719 Soulaïne, C., Gjetvaj, F., Garing, C., Roman, S., Russian, A., Gouze, P., & Tchelepi, H. A.
720 (2016). The impact of sub-resolution porosity of X-ray microtomography images on the
721 permeability. *Transport in Porous Media*, 113(1), 227–243.
- 722 Spurin, C., Bultreys, T., Bijeljic, B., Blunt, M. J., & Krevor, S. (2019). Intermittent fluid
723 connectivity during two-phase flow in a heterogeneous carbonate rock. *Physical Review*
724 *E*, 100(4), 1–10. <https://doi.org/10.1103/PhysRevE.100.043103>
- 725 Sun, C., McClure, J. E., Mostaghimi, P., Herring, A. L., Meisenheimer, D. E., Wildenschild,
726 D., et al. (2020). Characterization of wetting using topological principles. *Journal of*
727 *Colloid and Interface Science*, 578, 106–115.
- 728 Wang, S., Ruspini, L. C., Øren, P. E., Van Offenwert, S., & Bultreys, T. (2022). Anchoring
729 Multi-Scale Models to Micron-Scale Imaging of Multiphase Flow in Rocks. *Water*
730 *Resources Research*, 58(1), 1–16. <https://doi.org/10.1029/2021WR030870>
- 731 Zankoor, A., Khishvand, M., Mohamed, A., Wang, R., & Piri, M. (2021). In-situ capillary
732 pressure and wettability in natural porous media: Multi-scale experimentation and
733 automated characterization using X-ray images. *Journal of Colloid and Interface*
734 *Science*, 603, 356–369.
- 735 Zhang, X., Crawford, J. W., Flavel, R. J., & Young, I. M. (2016). A multi-scale Lattice
736 Boltzmann model for simulating solute transport in 3D X-ray micro-tomography images
737 of aggregated porous materials. *Journal of Hydrology*, 541, 1020–1029.
- 738